Power-Efficient ELF Wireless Communications Using Electro-Mechanical Transmitters

JARRED S. GLICKSTEIN[1], (Student Member, IEEE), **JIFU LIANG**[1], (Member, IEEE),
SEUNGDEOG CHOI[2], (Senior Member, IEEE),
ARJUNA MADANAYAKE[3], (Senior Member, IEEE),
AND SOUMYAJIT MANDAL[1], (Senior Member, IEEE)

[1]Department of Electrical Engineering and Computer Science, Case Western Reserve University, Cleveland, OH 44106, USA
[2]Department of Electrical and Computer Engineering, Mississippi State University, Starkville, MS 39762, USA
[3]Department of Electrical and Computer Engineering, Florida International University, Miami, FL 33174, USA

Corresponding author: Jarred S. Glickstein (jarred@case.edu)

ABSTRACT Ultra-miniaturized and highly power-efficient ELF (0.3-3 kHz) transmitters are desirable for underground and undersea wireless communications. This paper proposes the use of rotating permanently polarized dipoles (magnets or electrets) for such applications. A power-efficient data modulation scheme based on continuous-frequency FSK (CF-FSK) is also proposed for such electro-mechanical transmitters. Theoretical analysis and simulations show that 7-ary CF-FSK is optimal in the sense that it minimizes average mechanical torque on the mechatronic antenna for a given bit rate. Preliminary experimental results from a prototype ELF magnetic-field based transmitter based on a high-strength rare-earth (NdFeB) magnet and small brushless DC (BLDC) motor are presented. The results highlight local environment challenges such as power line interference that affect the choice of data encoding and modulation schemes. Reliable non-line-of-sight (NLOS) communication through concrete barriers at 100 Hz and ~0.25 bit/sec is demonstrated at distances up to ~5 m. The proposed mechatronic antenna and modulation scheme can be scaled up in both frequency and transmit power for more challenging applications in surface-to-undersea, surface-to-cave, and other conductive environments that require ELF channels.

INDEX TERMS Antennas and propagation, communication systems, electromechanical devices, emergency services, magnetic devices, transmitters.

I. INTRODUCTION

Wireless communications between the earth's surface and underground or deep-water facilities (mines, shelters, storage areas, tunnels, submarines, undersea cables, etc.) is very difficult due to the short skin depth δ of electromagnetic (EM) waves within conductive media such as earth or seawater, which leads to high attenuation. Fortunately, $\delta \propto 1/\sqrt{\omega}$ where ω is the frequency. Thus, extremely low frequency (ELF) EM waves can penetrate long distances in RF-denied environments [1]. Note that for convenience, here we use ''ELF'' as shorthand for the combination of the ELF, SLF, and ULF ranges (3-30 Hz, 30-300 Hz, and 0.3-3 kHz, respectively), for which EM wavelengths range from $10^5 - 10^2$ km in air. For example, the skin depth in sea water (conductivity $\sigma \approx 5$ S/m) is $\delta = 7.1$ m at 1 kHz, which

allows undersea communications to depths of ~30 m with reasonable transmit power levels [2].

The availability of portable low-power ELF transceivers would immediately enable communications within such RF-denied environments by enabling bidirectional low-data-rate wireless links with the surface. Promising applications of such transceivers include oil and gas exploration, search and rescue missions (cave rescues including when there is significant bodies of water in the signal path underground), biosensing (e.g., of marine and underground lifeforms), underwater and underground Internet of Things (IoT) networks (e.g., for ocean pollution monitoring and soil sensing), inter-submarine and submarine to surface wireless links, underwater autonomous robotics, advanced marine biology experiments, geophysics (e.g., subsurface imaging for locating geological conductors, such as ore deposits) [3] and atmospheric science (e.g., studies of the ionosphere) [4], [5]. The resulting near-field links have $\vec{E}$ and

The associate editor coordinating the review of this manuscript and approving it for publication was Cunhua Pan.

$\vec{B}$ fields that propagate independently; here we analyze and experimentally demonstrate magneto-inductive (MI) digital wireless links [6] based only on $\vec{B}$ fields, because magnetic fields are much less shielded than $\vec{E}$ fields by dielectric objects in the medium [7].

However, near-field ELF links present several problems, including i) limited bandwidth due to the use of low frequencies, which in turn limits channel capacity; and ii) the need to use electrically small antennas due to device size constraints. Fundamentally, the Chu-Harrington limit [8]–[10] lower-bounds the quality factor (Q) of small antennas to $\sim (c/\omega a)^3$, where a is the radius of its enclosing sphere, As a result, the bandwidth and radiation efficiency of small dipoles both degrade rapidly with frequency (as $\omega^4 a^3$ and $\omega^{3/2} a$, respectively), while small loops are even worse [2]. Thus, extremely large transmit antennas are necessary for obtaining reasonable bandwidth, channel capacity, and radiation efficiency at ELF [11]–[13]. ELF receivers can avoid similar issues by relying on noise matching (rather than impedance matching) to get high sensitivity. In particular, broadband noise matching is possible even for high-Q source impedances [14], which allows ELF receivers with modestly-sized antennas to obtain excellent sensitivity (< 0.1 fT/Hz$^{1/2}$) over a broad frequency range [15]–[17]. Thus, miniaturized and highly-sensitive ELF receivers are available, while far-field transmitters remain physically large and extremely power-hungry. Fortunately, the issue of poor radiation efficiency can be avoided in the near-field, where the radiated fields are small compared to the stored fields. In fact, various switching-based direct antenna modulation (DAM) schemes have been proposed for decoupling the efficiency, bandwidth, and Q of near-field antennas [18], [19]. Hence this paper focuses on miniaturized near-field ELF transmitters, which are the key for realizing short-range (up to ~ 1 km) bidirectional wireless links in conductive media.

Since near-field transmitters are not limited by antenna bandwidth or Q, the key issue for practical implementations is simply *field generation efficiency*, which is defined as the magnitude of $\vec{B}$ per unit power consumption at a given distance r, and has units of T/W. Modern ferromagnetic and ferroelectric materials (permanent magnets and electrets, respectively) have extremely high energy density and display strong permanent dipole moments, which makes them promising for achieving high field generation efficiency [1]. For example, let us compare a cylindrical NdFeB grade N52 magnet (remanent field $B_r = 1.5$ T, length = radius = 10 cm) with a N-turn current loop of the same cross-sectional area. In order for the two to generate the same static $\vec{B}$ field, the loop needs to carry a very large DC current of $\sim 10^5/N$ A. Hence, while the static magnet consumes no power, we estimate that even a tightly-packed copper loop will consume > 4 kW. Superconducting coils would eliminate the power dissipation problem, but modulating their persistent current in order to transmit data would then become highly challenging.

These facts suggest a fundamentally new approach to ELF transmitter design in which oscillating $\vec{B}$ fields (similar to those from oscillating electrical currents inside conductors) are generated by periodic mechanical motion of a magnet or electret. This "all-mechanical transmitter" approach is more power-efficient at low frequencies than conventional electrical transmitters, as analyzed in our earlier work [1], [2]. It also differs from early electromechanical transmitters, which simply coupled high-frequency AC generators (e.g., the Alexanderson alternator [20]) to dipole or loop antennas.

Electro-mechanical ELF transmitters have received significant academic attention since the concept was first described in 2017 as part of the DARPA AMEBA program [21]. Prototypes of transmitters based on rotating magnetic dipoles were demonstrated in [22], [23]. In both cases, the authors measured near-field antenna patterns and dependence of signal strength versus distance, but did not discuss data transmission. Other work has demonstrated all-mechanical very low frequency (VLF) transmitters by using piezoelectric elements to produce oscillating electric fields [24], [25]. The generated VLF electric fields have either directly been used to transmit information [24], or coupled to a magnetostrictive material to generate a magnetic field [25]. These works again pay a great deal of attention to design of the proposed antenna, but do not consider data transmission. In this paper, we emphasize suitable data modulation and encoding schemes, and also discuss how they influence the design requirements for ELF transmitters based on mechanically-rotating dipoles.

The paper is organized as follows: Section II presents a theoretical analysis of the proposed ELF transmitters. System design and data modulation are discussed in a theoretical context in Section III, and in an experimental context in Section IV. A prototype mechanical antenna is used in Section V to examine practical efficacy of the proposed data transmission system. Finally, Section VII concludes the paper and discusses directions for future work.

II. THEORETICAL ANALYSIS
A. FIELD GENERATION
The proposed ELF transmitters generate oscillating $\vec{B}$ fields by physically moving one or more static field sources. While in principle any type of periodic motion can be used, in practice mechanical challenges restrict the main choices to oscillations or rotations about a single axis [22]–[25]. Here we focus on rotating magnetic or electric dipoles, which have the highest possible field generation efficiency [2]. Various motion control methods can be used to implement electro-mechanical transmitters of this type. For example, spin transfer torques may be useful for implementing highly-miniaturized versions based on rotating nanoscale magnetic dipoles. However, in this paper we limit ourselves to larger devices, for which conventional electric motors are the obvious choice.

The $\vec{B}$ fields generated by rotating magnetic and electric dipoles have been thoroughly analyzed in our earlier work [2]. Here we summarize the main results.
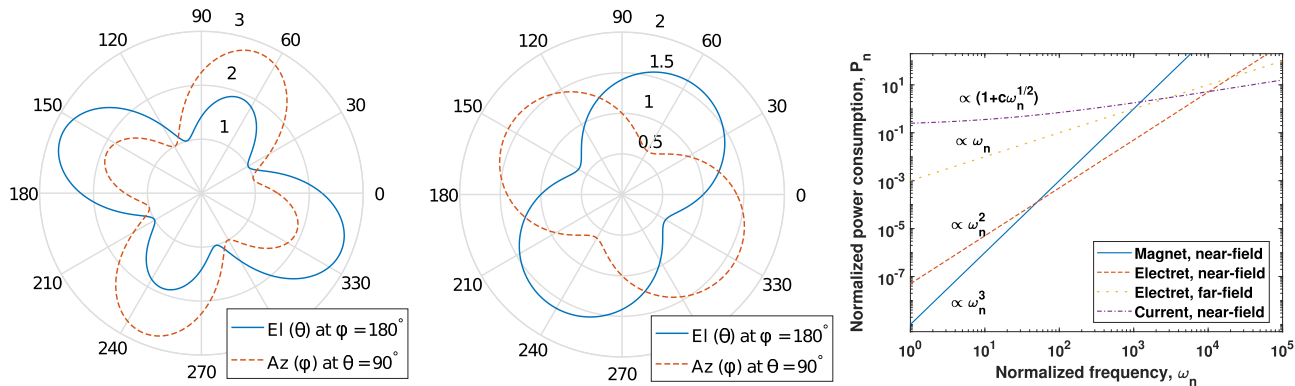
FIGURE 1. Theoretical near-field B-field patterns created by (a) a rotating magnetic dipole, and (b) a rotating electric dipole. In each case, elevation (El) and azimuth (Az) patterns of $|B_x + B_y + B_z|$ (the total amplitude measured by a 3-axis B-field sensor) are shown, where θ and ϕ denote the elevation and azimuth angles, respectively. (c) Qualitative comparison of the power consumed by different sources in order to generate the same B-field intensity at a given distance from an ELF transmitter. Rotating a magnet (near-field), electret (near-field), or electret (far-field) at ω results in a mechanical power consumption P that scales as ω^3, ω^2, and ω, respectively. On the other hand, using oscillating current in a loop as a magnetic dipole results in electrical power consumption P that scales as $(1 + c\omega^{1/2})$ where c is a constant; here the first term is due to DC resistance and the second due to skin effect.

1) ROTATING MAGNETIC DIPOLE

Consider a permanent magnet of volume V and remanent flux density B_r magnetized along the z-axis. The resulting dipole moment $\vec{m} = m\hat{z}$ where $m = B_r V / \mu_0$. Now assume that the magnet is rotated at a rate ω about an axis perpendicular to $\hat{z}$ (such as the x-axis) to generate an oscillating $\vec{B}$ field. The resulting dipole moment is circularly polarized and given by $\vec{m(t)} = m\sin(\omega t)\hat{y} + m\cos(\omega t)\hat{z}$, i.e., the sum of two oscillating dipoles [2]. The quasistatic approximation is valid in the near-field, i.e., at distances r for which $\omega \ll c/r$ and $kr \ll 1$, where $k = w/c$ is the wavenumber. The field in this region is then given by

$$\overrightarrow{B_{dip,rot}} = \frac{\mu_0}{4\pi} \frac{m}{r^3} \frac{3}{2} \sum_{l \in \{x,y,z\}} [a_l \cos(\omega t) + b_l \sin(\omega t)] \hat{l}, \quad (1)$$

where $a_x = \cos(\phi)\sin(2\theta)$, $a_y = \sin(\phi)\sin(2\theta)$, and $a_z = \frac{1}{3} + \cos(2\theta)$, $b_x = \sin(2\phi)\sin^2(\theta)$, $b_y = 2\sin^2(\phi)\sin^2(\theta) - \frac{2}{3}$, $b_z = a_y$, and θ and φ are the elevation and azimuth angles, respectively. Rotating magnetic dipoles behave as relatively omnidirectional sources, as shown in Fig. 1(a). All three field components oscillate in phase, so they can be easily summed up by a multi-axis receiver coil to generate the total field amplitude $|B_x + B_y + B_z|$, which has a maximum value given by $|B_{dip,rot}| = (3\sqrt{3} + 1)B_r V / (8\pi r^3)$.

2) ROTATING ELECTRIC DIPOLE

An electric dipole p_0 of volume V can also be rotated about an axis perpendicular to itself to generate an oscillating $\vec{B}$ field; typical values of remanent polarization $P_r = p_0/V$ for ferroelectric or piezoelectric materials are 20-50 μC/cm^2. The field due to the time-varying polarization vector $\hat{p} = p_0[\sin(\omega t)\hat{y} + \cos(\omega t)\hat{z}]$ is

$$\overrightarrow{B_{ed,rot}} = \frac{\mu_0}{4\pi} p_0 \omega (1 - ikr) \frac{e^{ikr}}{r^2}$$
$$\cdot \sum_{l \in \{x,y,z\}} [a_l \cos(\omega t) + b_l \sin(\omega t)] \hat{l}, \quad (2)$$

where $a_x = -\cos(\theta)$, $a_y = 0$, $a_z = \cos(\phi)\sin(\theta)$, $b_x = \sin(\phi)\sin(\theta)$, $b_y = -\cos(\phi)\sin(\theta)$, and $b_z = 0$. This function is the sum of a near-field term $\propto \omega/r^2$ which dominates when $kr \ll 1$, and a far-field term $\propto \omega^2/r$ which dominates when $kr \gg 1$. Thus, rotating electric dipoles also behave as relatively omnidirectional sources. However, the spatial distribution of total field amplitude $|B_x + B_y + B_z|$ is significantly different from the rotating magnetic dipole (see Fig. 1(b)). It has a maximum of $|\overrightarrow{B_{ed,rot}}| = \sqrt{3}(\mu_0\omega) P_r V / (4\pi r^2)$ (near-field) or $\sqrt{3}(\mu_0\omega^2/c) P_r V / (4\pi r)$ (far-field).

3) COMPARISON BETWEEN MAGNETIC AND ELECTRIC DIPOLES

The near-field generated by a magnetic dipole decreases with distance as r^{-3}, while that from an electric dipole decreases more slowly (as r^{-2} and r^{-1} in the near- and far-field, respectively). Also the former is frequency-independent, while the latter increases with frequency as ω and ω^2, respectively. Thus, electric dipoles are preferable for longer-range and higher-frequency applications.

4) EFFECT OF GROUND PLANES

The strength of the $\vec{B}$ field produced at the location of the receiver by a rotating dipole in air is effectively doubled by the presence of the Earth. At ELF frequencies with wavelengths beyond millions of meters, the Earth is an effective ground plane for communication from any reasonable elevation of the transmitter above mean sea level [23]. Therefore, the model developed in eqn. (1) for a dipole in free space predicts half the $B_{dip,rot}$ that is observed in practice as a result of the ground plane effect.

B. POWER CONSUMPTION

The peak electrical power input of a mechanical source is

$$P_{elec} = \frac{(\tau_f + \tau_{mod})\,\omega}{\eta_m \eta_e} = \left(\tau_f + J\frac{d\omega}{dt}\right)\frac{\omega}{\eta_m \eta_e}. \quad (3)$$

Here J is the total moment of inertia of all moving parts (magnet, bearings, and rotor), τ_f is the torque due to mechanical losses (air friction, bearing loss, etc.), and $\tau_{mod} = J(d\omega/dt)$ is the torque due to frequency modulation (used to transmit data). Also η_m and η_e are the efficiency of the motor and the drive electronics, respectively. The components of τ_f due to air friction and bearing loss scale as $\omega^2 V^2$ and ωV, respectively, where V is the volume of the source [26]. Thus the mechanical power consumption $\omega\tau_f$ required to generate a target $\vec{B}$-field magnitude increases rapidly with ω, although the increase is less rapid for rotating electric dipoles that generate stronger $\vec{B}$-fields as ω increases, which allows V to be reduced while keeping $|B|$ constant. Fig. 1(c) summarizes this analysis by showing qualitative estimates of the power required to generate a given $\vec{B}$-field amplitude using rotating magnetic and electric dipoles as a function of frequency (assuming the total source volume remains fixed). The power consumption of a conventional coil-based near-field transmitter is also shown for comparison. Clearly, mechanical transmitters are only beneficial up to a certain maximum operating frequency f_{max}. Next we discuss design methods to reduce the power consumption of all-mechanical transmitters, thus increasing the value of f_{max}.

1) SHAPE OF THE DIPOLE

The shape of the rotating source (magnet or electret) does not affect the dipole field, which only depends on volume V. Thus, we can reduce power consumption by minimizing J while keeping V fixed to maintain field strength. For example, axially-rotating cylinders of length l have $J = \rho V^2/(2\pi l)$, so J can be reduced by increasing the aspect ratio l/R of the cylinder while keeping V constant. Moreover, large aspect ratios also tend to reduce air friction. Thus, we focus on diametrically-polarized and axially-rotating cylinders with large aspect ratios as field sources. However, the resulting long and thin shapes are fragile and prone to mechanical instability during high-speed rotation (e.g., due to the advent of lateral oscillations) [27], [28].

2) DISTRIBUTED TRANSMITTERS

The strong dependence of inertia on physical size (e.g., $J \propto R^4$ for cylinders) suggests that *distributed transmitters* consisting of an array of small sources should be more power-efficient than a single large source of the same total volume. For example, consider dividing the source into $N > 1$ identical synchronously-rotating elements that are scaled down as $R \propto N^{-1/2}$ to keep the overall volume V constant. In this case, J per array element decreases as V^2/N and torque due to air friction decreases as $1/N^2$. The generated field per array element decreases as V/N, and thus overall field magnitude remains constant while the net power consumption P_{elec} decreases for the system of N elements. Thus, the effects of mechanical inertia on the system are reduced. Moreover, such distributed transmitters also provide built-in redundancy and robustness to localized failures. It is
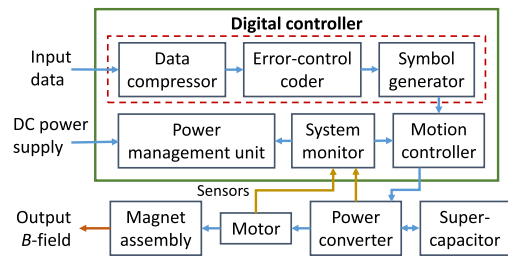

FIGURE 2. Proposed system design for transmitter producing $\vec{B}$-field signals from supplied input data.

worth noting that we do not consider such distributed transmitters to be useful as phased arrays. This is because the very long wavelengths at ELF (e.g., 10^5 m at 3 kHz in air) ensure that even km-scale arrays have sub-wavelength apertures. As a result, the fields from individual sources simply add in phase.

3) INTERACTIONS BETWEEN ROTATING DIPOLES

One challenge with using distributed transmitters is the dipole-dipole coupling between nearby sources, which increases power consumption by creating an additional *coupling torque* τ_c that must be supplied by the motors. For example, in the prototypical case of identical magnets of moment m separated by a distance $d = d\hat{z}$ and rotating synchronously about the x-axis, the coupling torque is

$$\vec{\tau_c} = \vec{m} \times \vec{B} = \frac{3\mu_0 m^2}{8\pi d^3} \sin(2\omega t)\hat{x}, \qquad (4)$$

which fluctuates sinusoidally at a frequency 2ω while decreasing with distance as $1/d^3$. Coupled electrets with a dipole moment p behave similarly: the resulting torque is the same as eqn. (4) once $\mu_0 m^2$ is replaced with p^2/ϵ_0.

While the analysis above predicts that τ_c oscillates at a frequency of 2ω in both cases, in practice the fluctuations in τ_c are random since ω is modulated to transmit data [2]. Fortunately, much of the electrical power required to supply such quasi-oscillatory torques can be recovered by using regenerative braking methods [29]. Nevertheless, the motor drivers must be appropriately sized to handle the rapidly-fluctuating peak power requirements.

III. SYSTEM DESIGN
A. DATA MODULATION
A block diagram of a single-element electro-mechanical ELF transmitter is shown in Fig. 2; distributed designs will be considered in later work. Most of the design complexity resides within the digital controller, which i) performs power management functions, ii) generates the modulation waveform given the input data, and ii) controls the motion of the field source (assumed to be a cylindrical permanent magnet) through a DC-AC power converter (inverter) and motor driver.

The data modulation scheme, which is shown within the dashed box in Fig. 2, is the focus of much concern in the design of power-efficient ELF communications. The proposed scheme should address the fundamental problem of power-efficient control of a mechanical device with high inertia and stored energy. We define efficient modulation schemes as those which minimize the additional torque τ_{mod} required by the motor to maintain the desired bit rate R_B. Given R_B, we then wish to minimize the symbol rate R_S by maximizing the number of bits within each symbol. Continuous phase modulation (CPM) methods such as continuous-phase frequency shift keying (CP-FSK), Gaussian minimum shift keying (GMSK), and shaped-offset quadrature phase-shift keying (SOQPSK) are promising for this purpose. The resulting waveforms have i) continuous phase, which results in high spectral efficiency and low out-of-band emissions, and ii) a constant envelope (CE), which maximizes power efficiency [30]. In addition, rotating dipoles naturally generate CE waveforms; therefore, CPM is well matched to the physical constraints of electro-mechanical transmitters. However, the initial phase of each CPM symbol depends on the earlier ones (i.e., the symbols have phase memory), which makes the design and implementation of an optimal receiver more complicated. The optimum receiver operates by detecting sequences of symbols, rather than on a bit-by-bit basis [31]. Fortunately, the necessary methods for detecting sequences, such as maximum likelihood sequence estimation (MLSE) using the Viterbi algorithm, are well known and can be readily implemented at the low data rates (< 1 kbps) supported by ELF links.

B. MINIMIZING POWER CONSUMPTION

Our proposed approach to enable power efficient and highly-miniaturized wireless ELF data transmission consists of two steps. The first is source coding to compress the data by removing redundancy. The second is to minimize the modulation torque τ_{mod} and associated power $\omega\tau_{mod}$ supplied by the motor while maintaining the desired bit rate R_B.

1) DATA COMPRESSION

The total energy required to transmit a given message within a specified time can be reduced by compressing the source data, which in turn reduces the necessary bit rate R_B. For example, consider DEFLATE, which is a well-known lossless data compression algorithm used in PNG images, ZIP files, etc. [32]. DEFLATE is a computationally-efficient scheme that combines the Lempel-Ziv algorithm (LZ77) [33] with Huffman coding to compress typical plain text by $\approx 3\times$. However, DEFLATE operates on data encoded in ASCII which requires 8 binary bits per character. To further compress the input message, a reduced character set is implemented consisting of numbers 0-9, letters A-Z, and a limited set of punctuation (space, comma, period, semicolon, exclamation mark). Using this reduced set of at most 49 characters, only 6 binary bits are required per character. Nevertheless, DEFLATE is written to operate on ASCII data; thus we expect

further improvements in compression ratio by using specialized compression algorithms that make effective use of the proposed reduced character set. Such a scheme is described in Section III-D.

2) MODULATION WAVEFORM

Energy consumption can be further reduced by packing multiple bits within each symbol to decrease the symbol rate R_S. In earlier work, we developed a multiple frequency-shift keying (MFSK)-based scheme for this purpose [1]. MFSK is a M-ary orthogonal modulation scheme in which M is the size of the alphabet (number of frequencies) and each symbol represents $\log_2(M)$ bits, resulting in $R_S = R_B/\log_2(M)$. However, a standard MFSK waveform has discontinuous phase $\varphi(t)$ due to rapid jumps between the symbols, which results in large spikes in the instantaneous frequency $\omega(t) = d\varphi(t)/dt$. CP-FSK is a well-known variant of MFSK that keeps $\varphi(t)$ continuous, i.e., eliminates frequency spikes by generating a CPM waveform [34].

A generic M-ary CPM waveform $s(t)$ is defined as

$$s(t) = A_c \cos(\omega_0 t + 2\pi \sum_{i=0}^{n} \alpha_i h_i q(t - iT)), \qquad (5)$$

where amplitude A_c is a constant proportional to the dipole moment; $T = \frac{1}{R_S}$ is the symbol period; α_i are the $\log_2(M)$-bit data symbols; h_i is the modulation index (which can vary from symbol to symbol in multi-h schemes); and $q(t)$ is the *phase response function*. CPM schemes can be classified using $q(t)$ or its derivative $\frac{dq}{dt} = g(t)$, which is known as the *frequency response function*. For example, LRC and $LREC$ schemes use raised cosine and rectangular frequency pulses of length L symbols, respectively. The term CP-FSK refers to $LREC$ schemes with $L = 1$ that define $g(t)$ to be $1/(2T)$ for $0 < t < T$ and zero otherwise. Thus, they are commonly referred to as $1REC$, denoting CPM schemes with rectangular frequency pulses of length T and phase memory $g(t)$ communicated across one symbol. CP-FSK waveforms are continuous, but the symbols are not orthogonal unless h is a multiple of $\frac{1}{2}$.

In order to understand the properties of CP-FSK, it is useful to first consider a conventional MFSK waveform $s(t)$, which is defined as

$$s(t) = A_c \cos(\omega_0 t + 2\pi \Delta f \times m(t)). \qquad (6)$$

Here $m(t)$ is the digital data to be transmitted, Δf sets the frequency steps between symbols, and ω_0 is an integer multiple of Δf to ensure orthogonality between them. Signals for which $m(t) \in [0, 1]$ result in binary FSK, where each symbol contains a single bit. Similarly, signals for which $m(t) \in [0, M - 1]$ result in MFSK.

By contrast, a M-ary CP-FSK waveform is defined as

$$s(t) = A_c \cos\left(\omega_0 t + 2\pi \Delta f \int_0^t m(t_1) dt_1\right), \qquad (7)$$

where all terms remain as previously defined. Comparing eqns. (5) with (6), we see that the instantaneous phase

modulation driven by $m(t)$ is replaced with an integral that defines the phase response function. This integral ensures that $\varphi(t)$ remains continuous (as required for a CPM waveform), but discontinuities remain in its derivative $d\varphi(t)/dt = \omega(t)$. As a result, large spikes occur in both the angular acceleration $\alpha(t) = d\omega(t)/dt$ and modulation torque $\tau_{mod}(t) = J\alpha(t)$. As described in [1], these can be removed by low-pass filtering the integral before phase modulation, resulting in

$$s(t) = A_c \cos\left(\omega_0 t + 2\pi \Delta f \times (n * h)(t)\right), \quad (8)$$

where $h(t)$ is the impulse response of the low-pass filter (LPF) and $n(t) \equiv \int_0^t m(t_1)dt_1$ is the filtered version of $m(t)$. This continuous-frequency FSK (CF-FSK) scheme ensures that both $\varphi(t)$ and $\omega(t)$ remain continuous, which in turn ensures that $\alpha(t)$ and τ_{mod} remain finite. The choice of $h(t)$ is relatively arbitrary. For example, we can use a boxcar function $h(t) = rect(t/T_S)/T_S$ of width $T_S = 1/R_S$, which corresponds to a sinc function in the frequency domain. This particular filter is interesting because it keeps $\omega(t)$ piecewise linear, which in turn simplifies motor design by restricting $\tau_{mod}(t)$ to a finite set of values.

The value of $\alpha(t)$ decreases along with Δf. However, reducing Δf eventually destroys orthogonality between the symbols, which increases the bit error rate (BER). Assuming coherent or noncoherent detection, the minimum step size that ensures orthogonality is known to be $\Delta f = R_S/2$ or R_S, respectively, for CP-FSK. For simplicity, we assume the same limit for CF-FSK.

Assuming constant Δf, increasing the number of symbols M also increases the torque required to transmit a message. Increasing the number of symbols increases the maximum and rms values of $m(t)$, thereby increasing the required rms motor acceleration (and therefore power) to transmit a symbol. However, each symbol represents $\log_2(M)$ bits and so increasing the number of levels increases the number of bits per symbol, thus decreasing the number of symbols required to transmit the same message. This trade-off results in an optimum value of M that minimizes the power required to transmit a fixed-length message.

The rms value of $\alpha(t)$ over the message duration, which sets the peak motor power rating, is represented by σ_α. Assuming the transmitted data is random, the rms angular frequency step is $\sigma_{\Delta\omega} = 2\pi \times \Delta f \times \sigma_D$, where σ_D is the rms value of the transmitted data values D. Since the symbol duration $\Delta t \equiv 1/R_s = 2/\Delta f$ for coherent detection and $\alpha(t) = d\omega(t)/dt = \Delta\omega/\Delta t$, σ_α is given by

$$\sigma_\alpha = \pi R_s^2 \sigma_D. \quad (9)$$

Each symbol represents $\log_2 M$ bits, so σ_α in terms of the bit rate R_B is given by

$$\sigma_\alpha = \frac{\pi R_B^2 \sigma_D}{(\log_2(M))^2}. \quad (10)$$

If we assume that each symbol is equally probable, σ_D can be approximated as $M/\sqrt{12}$ for $M \gg 1$. The normalized acceleration $\sigma_\alpha/(2\pi R_B^2)$ as a function of M predicted by an
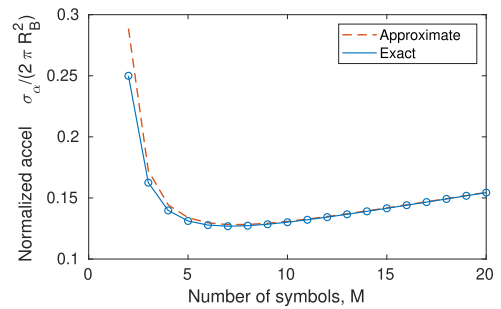
FIGURE 3. Normalized value of rms angular acceleration versus the number of CF-FSK symbols.
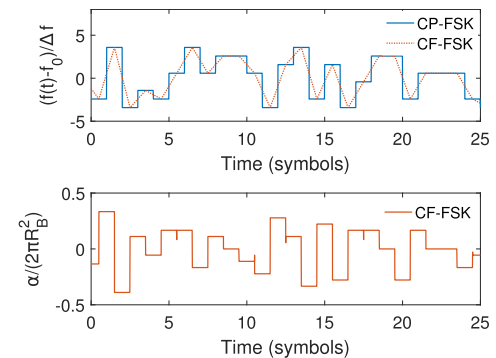
FIGURE 4. Simulated instantaneous frequency offset (top) and modulation rate (bottom) for CP-FSK and CF-FSK, both with $M = 8$.

exact calculation of σ_D as well as the approximation is shown in Fig. 3. The optimal value is $M = 7$, which results in a $2\times$ reduction in σ_α compared to binary modulation ($M = 2$).

C. SIMULATION RESULTS
Simulated CP-FSK and CF-FSK waveforms generated by the same random data stream are shown in Fig. 4. CF-FSK limits σ_α to $0.152 \times 2\pi R_B^2$, which is within 15% of the theoretical result. Fig. 5 compares the power spectra of the two schemes estimated using Welch's method [35]. The figure shows that the transmitted bandwidth B_S is slightly smaller for CF-FSK than CP-FSK. The bandwidth for both schemes can be approximately derived by using Carson's rule for frequency modulation [36], which states that for $\Delta(f) \ll f_0$, $B_S \approx (M\Delta f + 2f_m)$, where f_m is the bandwidth of the input signal. In our case $f_m \approx R_S/2 = \Delta f$; we therefore expect that $B_S \approx (M + 2)\Delta f = 10\Delta f$ for $M = 8$, which agrees with the simulation results shown in Fig. 5.

D. DIFFERENTIAL CODING
The proposed M-ary CPM scheme can be combined with differential coding to provide several benefits over conventional FSK. Each symbol α_i in such an M-ary scheme has a value in the range $\alpha_i \in [0, M-1]$ for M unique data symbol values. To increase the number of bits transmitted per symbol, differential encoding is applied in a manner similar to differential phase shift keying (DPSK). In a differential scheme, data is transmitted as the change from interval to interval rather
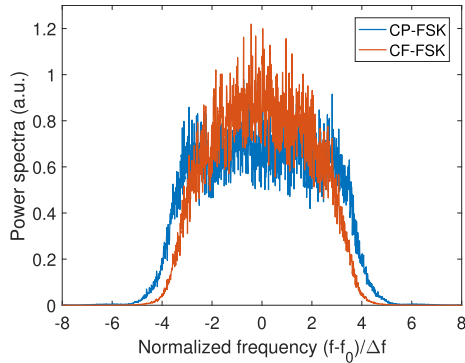
FIGURE 5. Simulated power spectra of the transmitted waveforms for CP-FSK and CF-FSK, both with $M = 8$.

than as the intervals themselves [30]. For example, DPSK is a binary scheme in which the symbols are encoded by the transformation

$$\alpha_i = |m(t_i) - m(t_{i-1})| \qquad (11)$$

A message transmitted with M-ary FSK requires a bandwidth $\Delta f (M - 1)$ in the receiver as there are M fixed-frequency levels which must be observed by the receiver. However, consider the case of CPM for the same value of M. Differential modulation schemes require the use of a special *differential detector*. For the case of DPSK, note the differential detector discards the sign of the difference between present and previous transmitted bits and records only the magnitude. For the proposed CP-FSK modulation scheme, using a differential detector sensitive to the magnitude as well as the sign of each transition, each symbol may take a value in the range $[-\frac{M-1}{2}, \frac{M-1}{2}]$. As a result, the required bandwidth for the transmission of M unique data symbols is only $\frac{1}{2}\Delta f (M - 1)$. Thus, the required bandwidth for M unique symbols transmitted using M-ary CP-FSK (or CF-FSK) is half that of conventional FSK.

This type of differential coding is impractical to implement in conventional FSK as sign-sensitive differential detection of non-random data will inevitably require the transmission of long sequences of positive or negative values. In either case, no more data of the same sign may be transmitted once the magnitude $|m(t_{i-1})| = M - 1$. The situation could be corrected by constructing a differential detector sensitive to transitions $m(t_i) - m(t_{i-})$ rather than $m(t_i) - m(t_{i-1})$ and adding additional frequency shifts within the transmit signal to code transitions which accumulate too great a net frequency shift over time. This frequency shift would be indistinguishable from a data transition in conventional CF-FSK modulation schemes, only it would occur some time within a symbol period. It is then critical that the differential detector is sensitive only to transitions at the data clock edge and not within the symbol period, otherwise frequency discontinuities introduced to transmit successive differential-coded transitions of the same sign would be falsely detected as individual bits. In the proposed CF-FSK modulation scheme of Fig. 4, differential coding correction frequency shifts could be near

instantaneous compared with the slow continuously-time-varying frequency of each actual transition. A differential detector is readily adaptable to such a signal.

The differential detection scheme introduces some memory to the signal as each received bit depends on both the present and previous received values ($m(t_i)$ and $m(t_i)$, respectively). As a consequence, one error in transmission produces two received bit errors, which doubles the BER [30]. The proposed CP-FSK scheme avoids increases in BER due to differential coding, as the differential detector uses the trajectory of the received signal rather than discrete present and previous values to determine the value of each bit. The phase memory introduced by the modulation scheme may then be used as additional information to increase the confidence of the detector in selecting the most probable current symbol.

E. BIT ERROR RATE (BER) ANALYSIS

The BER analysis of CPM schemes is relatively complex. For the simplest case of an additive white Gaussian noise (AWGN) channel, the error probability of a maximum likelihood (ML) receiver for the i-th transmitted symbol $s_i(t)$ is bounded by

$$P_{be}(i) \leq \sum_{k \neq i} Q\left(d_{i,k}\sqrt{E_b/N_0}\right), \qquad (12)$$

where $d_{i,k}$ is the Euclidean distance between $s_i(t)$ and the erroneous detected symbol $s_k(t)$; $E_b = A_c^2 T / (2 \log_2(M))$ and N_0 are the energy per bit and noise power spectral density, respectively; and $Q(x) = \frac{1}{2}[1 - \text{erf}(x/\sqrt{2})]$ where $\text{erf}(x)$ is the error function [30].

The worst-case BER (i.e., upper bound) shown in eqn. (12) occurs when all $M - 1$ symbol errors are equally likely. Finding the upper bound is analytically difficult; instead, here we consider the lower bound. The latter can be derived by assuming that, though there are $M - 1$ possible ways to make an error per symbol, the receiver only makes the most likely errors, i.e., always selects the symbol that is "closest" to the transmitted one [31]. Experimental results confirm that this is a good approximation for the prototype ELF receiver. In this case the minimum possible value of $d_{i,k}$ (denoted as d_{min}) sets the error performance of the receiver, and the total BER is approximately

$$P_{be} \approx Q\left(d_{min}\sqrt{E_b/N_0}\right). \qquad (13)$$

The value of d_{min}^2 for the proposed CP-FSK modulation scheme is tabulated for some common values of M in [30, p. 66]. In particular, results are tabulated for $M = 4$ (quaternary) and $M = 8$ (octal) for various values of the modulation index h. The BER for the optimum case ($M = 7$) is expected to be bounded by these two cases; taking $h = 1$, in the worst case we expect $d_{min}^2 \approx 5.5$ for octal and $d_{min}^2 \approx 4$ for quaternary 1*REC* modulation. The resulting BER curves versus E_b/N_0 are shown in Fig. 6.

In practice, an AWGN model is not accurate for atmospheric, underground, and undersea ELF and VLF channels [15], [37]. Atmospheric noise at such low frequencies
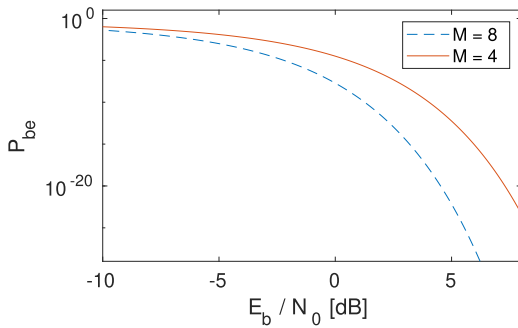
FIGURE 6. Theoretical BER performance of a CP-FSK receiver in an AWGN channel.

FIGURE 7. Estimated compression ratio performance of DEFLATE, BWT+RLE, and BWT+RLE+RCS algorithms on typical English text (five well-known novels) as a function of string length.

FIGURE 8. A labeled photo of the prototype mechanical transmitter. Controller electronics are not shown in the photo.

exhibits impulse-like "sferics" induced by lightning strokes from storms, and "chorus" or "hiss" emissions from the magnetosphere, respectively; additional noise sources include power line harmonics and ionospheric resonances. Many of these sources have time-varying and non-Gaussian probability distributions; they are also often correlated with fluctuations in the received signal amplitude (i.e., fading events). In addition to noise, underground and undersea propagation is frequency-dependent due to the dispersive medium. Thus, ELF channels exhibit both time- and frequency-dependent fading. The study of BER for CP-FSK or CF-FSK waveforms in such complex channels is left for future work.

F. DATA ENCODING

Fig. 3 shows that while $M = 7$ is the optimum number of CF-FSK symbols to minimize the torque due to modulation, the curve is nearly flat over the range $[4, 15]$. Moreover, the maximum frequency excursion for a given symbol rate is proportional to M. Regardless, we chose to use the optimum value $M = 7$. Assuming a differential detector, data with values in the range $[-3, 3]$ may thus be coded for transmission. This range is linearly mapped to $[0, 6]$ for convenience. The DEFLATE algorithm operates on messages encoded using the ASCII character set and requires one 8-binary-bit byte per character. Transmission of this data using the 7 available symbols would require 3-septenary-bit bytes to represent all 256 characters in the ASCII set. However, proposed applications for ELF transmitters do not necessarily require the entire ASCII character set to be available. By implementing coding of messages using a reduced character set (RCS) as described in Section III-A, the effective data rate may be increased by reducing the number of symbols used to represent each character.

Consider a case where symbols are grouped into two-bit bytes. The numbers 00 to 55 in base-6 correspond to the numbers 0-9 followed by the Latin letters A-Z in base-36. This observation offers a convenient way to encode real data while leaving 14 additional values (when either MSB or LSB is 6 in a byte) for punctuation, data compression, and error-checking codes. In this character encoding scheme, each character uses two bytes, resulting in an effective data rate that is increased by a factor of $1.5\times$ compared to transmission using the ASCII character set.
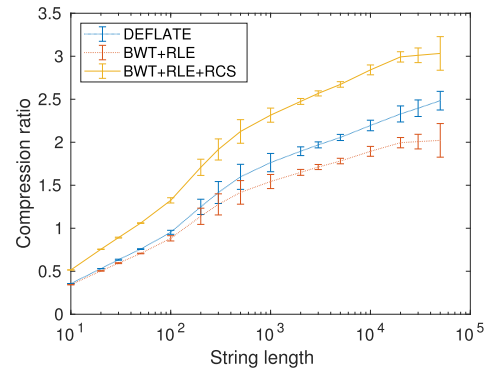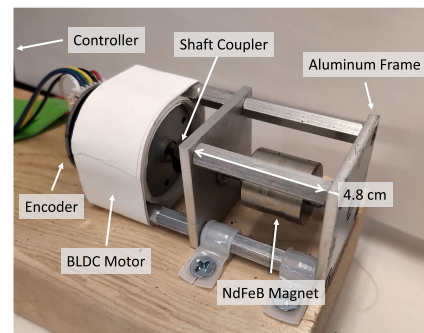
The DEFLATE algorithm has not yet been implemented for such a reduced character set, so an alternative compression algorithm is proposed which operates on any character set. A combination of the Burrows-Wheeler transform (BWT) and run-length encoding (RLE) is used to achieve comparable compression ratios to DEFLATE in a direct comparison on ASCII data shown in Fig. 7. The Burrows-Wheeler transform applies block-sorting to rearrange the input message in a way which increases the frequency of runs of identical characters. Then, run-length based compression is applied by replacing runs of identical characters in a string with one character followed by a counter to indicate how many times the bit is repeated. For example, a sequence such as "ABBBBC" may be replaced by "AB(3x)C". A single byte counter code is used to represent the counter "(3x)" to minimize the number of bytes in the transmission-ready signal. Simulation shows this algorithm alone achieves a slightly lower compression ratio than DEFLATE. However, implementing a reduced character set after BWT+RLE compression results in an effective compression ratio above the performance of DEFLATE.

IV. EXPERIMENTAL SETUP

An electro-mechanical transmitter designed to operate at ~100 Hz was realized using a small brushless DC (BLDC) motor which drives a magnet made of grade N42 neodymium
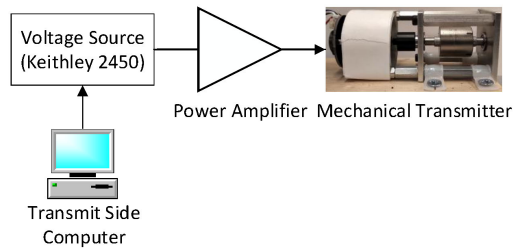
FIGURE 9. Block diagram of the transmitter side of the experiment.

FIGURE 10. Block diagram of the receiver side of the experiment.

FIGURE 11. Measured data at the input to the lock-in amplifier on the receive side at a location 4.67 m away from transmitter, shown (a) before, and (b) after the use of notch filters.

alloy (NdFeB) mounted to a shaft. The transmitter assembly is shown in Fig. 8. The motor is rated for a no-load speed of 10,000 rpm at 12 VDC, weighs 63 g, and is 34×33 mm ($L \times W$) in size with an output shaft 7.1×2 mm ($L \times D$). The magnet is a diametrically polarized ring with dimensions 19.05 mm outside diameter, 6.35 mm inside diameter, and 19.05 mm length. Given $B_r = 1.31$ T, the estimated magnetic moment is $m = 5.03$ Am^2. The complete assembly is $38 \times 38 \times 83$ mm ($H \times W \times D$) in size.

We now discuss design and control of the transmitter as well as an experimental setup for a receiver to test non-line-of-sight (NLOS) ELF communications. Following tests of transmitter capabilities, experimental data transmission results are shown and data encoding/decoding methods are developed to meet environmental restrictions on the wireless channel.

A. TRANSMITTER DESIGN

The motor for the transmitter is driven by a power amplifier (PA) (AE Techron 7224) in voltage-output mode with open-loop control signals provided by a programmable voltage source (Keithley 2450 source-measure unit [SMU]) as shown in Fig. 9. Initially, the voltage-frequency characteristic of the motor was experimentally determined. This calibrated relationship was then used to calculate the SMU input waveform necessary for encoding user-specified data using the CP-FSK and CF-FSK modulation schemes described in the previous section. Finally, the SMU was controlled from a computer over a GPIB bus in order to run an experiment. With a suitably high Δf between input levels (such as the 4 Hz used in the experiments which follow), errors from this open-loop control approach may conveniently be neglected. At low data rates (such as the 0.25-0.5 bits/sec used experimentally), GPIB communication latency may be neglected as well.

B. RECEIVER DESIGN

A block diagram of the receiver-side signal path is shown in Fig. 10. The receiver uses an inductive single-axis $\vec{B}$-field sensor (Magcheck-95 [MC95] from Magnetic Sciences), with a rated -3 dB magnitude bandwidth of 25 Hz to 3 kHz. Interference from power lines poses a challenge to ELF communications; in the United States, such interference has a fundamental frequency of 60 Hz. The initial goal was to transmit the signal between the strong 60 Hz and 120 Hz interference lines. Thus, the initial transmit signals used in testing had $M = 15$ symbols and $\Delta f = 4$ Hz between
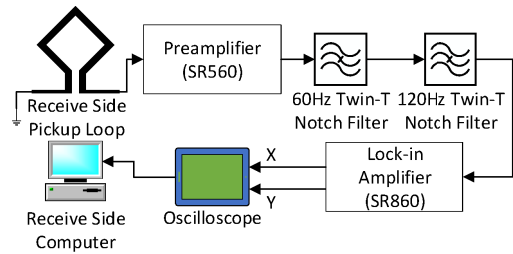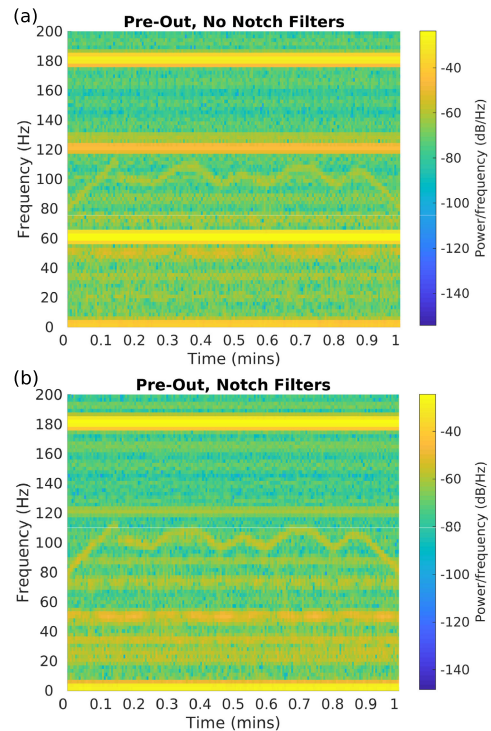
levels for a data bandwidth of 88-116 Hz; the sensitivity of the MC95 sensor is effectively constant at 1 mV/mG over this range. Initially the receive-side signal path simply consisted of a low-noise amplifier (LNA) (SR560, Stanford Research Systems) with programmable gain connected to an oscilloscope. However, the LNA did not have a sharp enough cut-off to filter power-line interference without removing the signal itself, so two active twin-T notch filters (tuned to 60 and 120 Hz, respectively) were added to attenuate these sources. However, while transmitting across a distance greater than several meters, the LNA was found to quickly saturate before enough gain could be attained. To achieve longer transmission distances, a lock-in amplifier (SR860, Stanford Research Systems) with extremely high sensitivity (up to 1 nv full-scale input range) was added after the notch filters. The LNA was then used as a low-gain preamplifier to set the input-referred noise floor and buffer the input to the notch filters.

Fig. 11 shows the spectrogram of a typical 10-bit CP-FSK sequence received with and without the use of notch filtering.
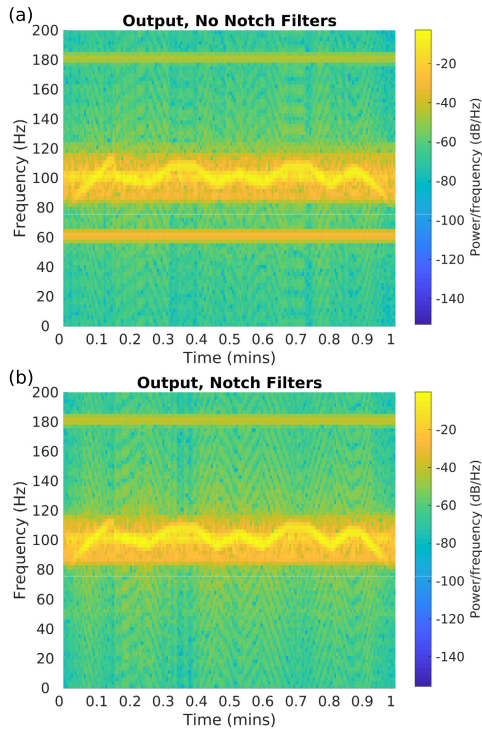
FIGURE 12. Measured data at the output of lock-in amplifier on the receive side at a location 4.67 m away from transmitter, shown (a) before, and (b) after the use of notch filters.

The most invasive noise is the second harmonic at 120 Hz, which is too close to the signal transmission bandwidth to be filtered out by the lock in amplifier. In Fig. 11(a) (without notch filtering), the LNA is set to a gain of 200, which was the highest achievable before 60 Hz noise saturated the input to the lock-in amplifier.

With the use of notch filters (see Fig. 11(b)), LNA gain could be increased to 500 before the input to the lock-in amplifier saturates, now by the third power line harmonic (180 Hz). The built-in filtering provided by the lock-in amplifier can reject this term, as shown in Fig. 12: The figure confirms that the third harmonic present at the lock-in output is significantly reduced (even for higher LNA gain) compared with Fig. 11. However, 180 Hz is still too close to the transmit signal bandwidth to be completely filtered out without also attenuating the transmitted signal. Thus, further improvements in receiver sensitivity are possible by using additional notch filters tuned to power line harmonics at 180 Hz, 240 Hz, etc.

V. EXPERIMENTAL RESULTS
A. FIELD STRENGTH VERSUS DISTANCE
In initial tests, the field strength versus distance d was measured at several points from 0.14 to 1.4 meters away from the transmitter. The motor speed was kept constant at 100 Hz (6,000 rpm) during these tests. The results, which are plotted in Fig. 13, confirm the expected field dropoff profile. In particular, the measured data is well fit by a function $\propto \frac{1}{d^3}$.
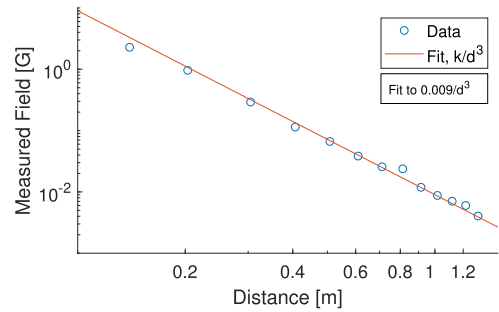

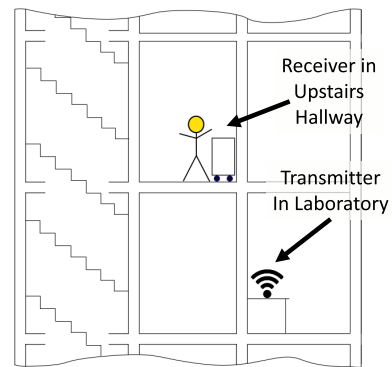**FIGURE 13.** Measured dependence of field strength versus distance at 100 Hz.

FIGURE 14. Graphic depicting the location of the prototype mechanical ELF transmitter and inductive receiver in an office building. This setup was used for data transmission in the following sub-sections.

The receiver pickup coil has a sensitivity of 1 mV/mG (i.e., 10^4 V/T) over the transmission operating bandwidth, while the SR560 pre-amplifier has a noise floor of 4 nV/Hz$^{1/2}$. These values correspond to a measurement sensitivity of 400 fT/Hz$^{1/2}$, which is adequate for these tests. However, $\sim 10^3$ times better sensitivity is possible using state of the art $\vec{B}$-field receivers in this frequency range, such as the AWE-SOME instrument [17]. Given that $B \propto 1/d^3$, using such a sensitive receiver would immediately increase the useful range of our transmitter by a factor of ~ 10.

B. WIRELESS NLOS DATA TRANSMISSION
In order to transmit data, various CP-FSK and CF-FSK waveforms were generated in the manner described in Section III-A. Using the experimentally determined frequency-voltage characteristic of the transmitter motor, transmit signals, such as those shown in Fig. 4, are converted to vectors of motor voltage corresponding to the desired transmit frequency. At low operating frequencies (typical center frequency of 100 Hz with $\Delta f = 4$ Hz) and data rates (typical symbol period of 2-4 sec), this rudimentary open loop control system is sufficient to demonstrate successful transmission of data.

Wireless NLOS communications using the mechanical transmitter was demonstrated by placing the receiver in a hallway one floor above the transmitter (see Fig. 14). The
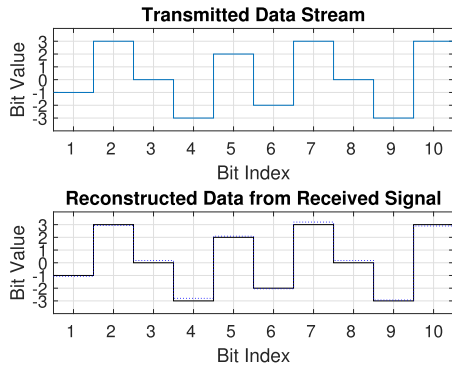
FIGURE 15. Computer-generated transmit data bit stream compared with data received from the prototype transmitter.
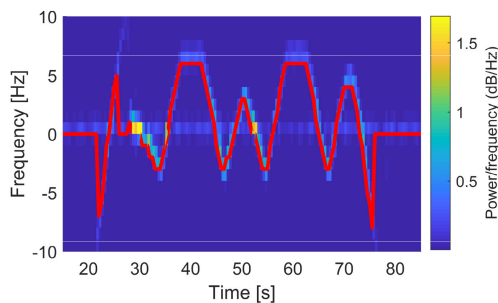

FIGURE 16. Received power spectral density (PSD) of the signal versus time (multicolored, background) with peak intensity (red line, foreground) used to recover the data.

receiver was installed on a mobile cart in order to observe the ambient noise at various locations in the hallway. At the default location, the distance between transmitter and receiver in this setup was approximately 4.67 m with the two separated by a wall and floor/ceiling. During the tests, transmit data bandwidth was reduced to 96-108 Hz by using $M = 7$ symbols and $\Delta f = 4$ Hz. This narrow bandwidth permits more selective (larger Q factor) bandpass filtering in the lock-in amplifier to reject ambient noise and power line harmonics, as described in Section IV-B.

Fig. 15 shows i) example transmit data used to generate a 10-symbol CP-FSK message ($\approx$28 binary bits), and ii) the reconstructed receive signal. The raw receive data values are plotted as a dashed line with the recovered bits shown as a solid line at the nearest valid bit value. The figure confirms successful data transmission.

The process of data recovery is now described. For convenience, we implemented a simple spectrogram-based decoder rather than the optimal MLSE-based decoder. Data was captured in the time domain and then post-processed using a short-time Fourier transform (STFT). Time windows of 1 s overlapping by 0.5 s result in an effective frequency resolution of 1 Hz and a time resolution of 0.5 s, and generate spectrograms as shown in Fig. 16. Unlike the simulated sequences, the transmitted signal also includes ramp-up and ramp-down features which reduce wear on the motor and function as transmission "start" and "stop" indicators.
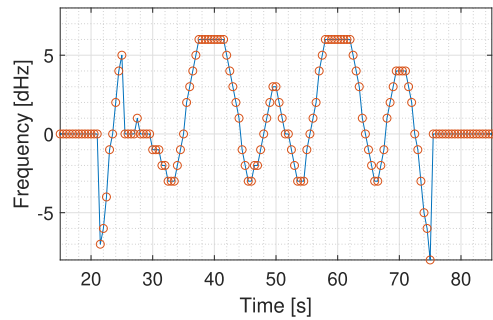

FIGURE 17. Measured peak PSD plotted to demonstrate how each symbol is windowed to recover the transmitted data.

Shown as a red trace in the figure is the peak of the PSD within each 0.5 s window, which is extracted to recover the transmitted signal.

The peak PSD shown in Fig. 16 is shown in Fig. 17, with data points plotted on top of the smooth curve for clarity. The 10-symbol transmit sequence has a symbol period of 4 s, resulting in 8 sample points per bit for STFT windows of duration 0.5 s. These data points are split into bit periods as shown by light blue traces in the figure. A piecewise linear fit is used to extract the bit value in each region. Note that the data shown has a dynamic range of -3 Hz to $+6$ Hz, while the transmitted waveform had a bandwidth -4 Hz to $+8$ Hz. This error is due to open loop motor control, and can be easily corrected by re-scaling this data before applying a linear fit since the received data still satisfies the condition $\Delta f \geq R_S = \frac{1}{T_S}$ for noncoherent detection, i.e., consists of an orthogonal set of symbols.

C. PRACTICAL MESSAGE TRANSMISSION
Practical transmission of data through the link has been demonstrated using a 233-character excerpt from Shakespeare's *Hamlet*, Act II, Scene 2:

```
WHAT A PIECE OF WORK IS MAN!
HOW NOBLE IN REASON,
HOW INFINITE IN FACULTY.
IN FORM AND MOVING,
HOW EXPRESS AND ADMIRABLE.
IN ACTION, HOW LIKE AN ANGEL.
IN APPREHENSION, HOW LIKE A GOD.
THE BEAUTY OF THE WORLD,
THE PARAGON OF ANIMALS.
```

The full data encoding scheme shown in Fig. 18 was developed from the data modulation theory of Section III-A and preliminary experimental results. It was applied to the input data to produce a suitable transmission-ready signal. Compression reduced the sequence of 233 characters to 208 characters, 89% of the original size. For demonstration purposes, parity was not implemented and is left for future work.

The sequence of 208 characters was represented by 416 symbols using the established data encoding system. With a symbol period of 4 seconds, this data is transmitted
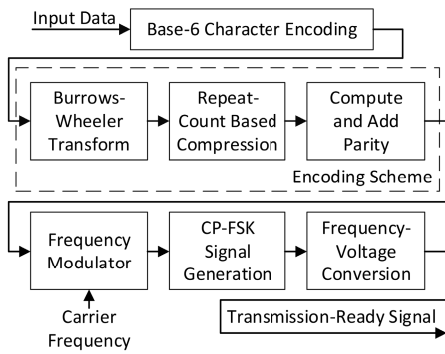
FIGURE 18. Data encoding scheme used with prototype transmitter taking input data as a string of characters to produce a transmission-ready signal with compression and error-checking.
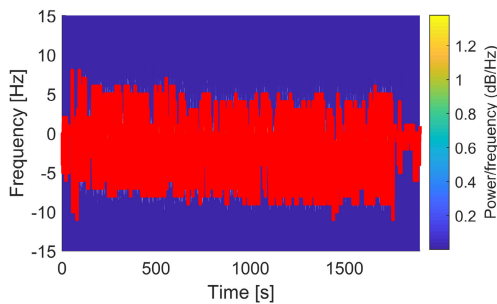

FIGURE 19. Spectrogram of the received signal showing slow drift in transmission frequency over time.

FIGURE 20. Data decoding scheme used to recover the message from received data.

FIGURE 21. Sample section of received CP-FSK signal with critical features and one error shown as an example.

FIGURE 22. Sample sequence of bits from message transmission experiment showing comparison between transmit and receive signals.

in 1664 seconds (about 28 minutes). The spectrogram of data from the entire experiment in Fig. 19 shows an interesting consequence of open-loop voltage control. In a long transmission the transmitter bandwidth shifts, presumably as the motor heats up and coil impedance changes. Using a current source or switching to closed loop control in future work is proposed to correct this problem.

Received data is processed using a demodulation scheme to recover the received message from the quadrature receive signal input to the block diagram of Fig. 20. The peak short time PSD of the entire received message is shown in Fig. 19 above. Windowing is applied to the peak PSD to identify the start and length of each symbol using the known symbol period and maximum rate of change in frequency. The piecewise linear fit produces a goodness of fit metric (R^2) which is used to determine whether the symbol window is reasonable.

Limited time resolution and errors present at transitions between symbols result in bit windows being less than the theoretical 9 samples which would represent a range of 4 seconds at 0.5 second intervals. In the absence of a clock signal, critical features such as peaks and discontinuities are used to identify the start position and length of each bit. These features are highlighted in Fig. 21, a sample 10 symbol sequence from the received message. This sequence also contains an error at index 378. The receive data decoding scheme of Fig. 20 shows two methods proposed to detect such an error. Using goodness of fit to detect an improperly
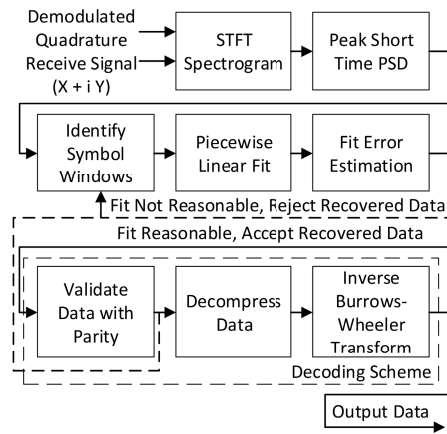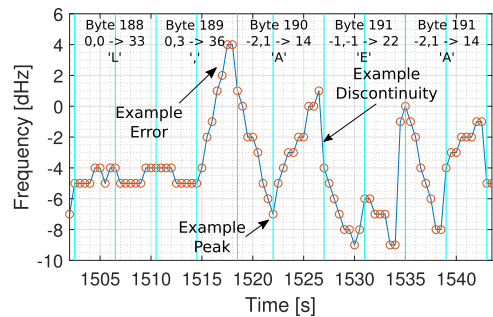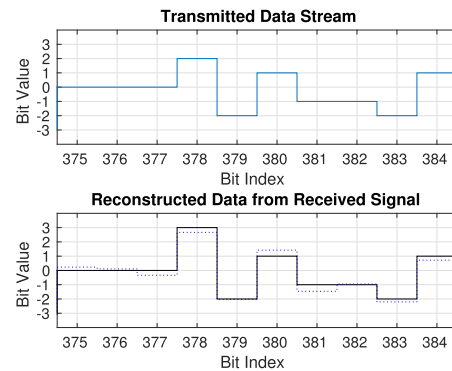
windowed bit would not correct this data as this bit has a smooth profile and the linear fit computed goodness of fit is 0.9932. Implementing parity would allow for this error to be detected but not corrected. In either case, re-transmission of some data is required.

A short sequence of 10 symbols in the decoded receive signal is shown in Fig. 22. This sequence is chosen to correspond to the sequence shown in Fig. 21. In the transmission of 416 symbols, the error shown is the only erroneous symbol in the sequence. With retransmission of the short sequence
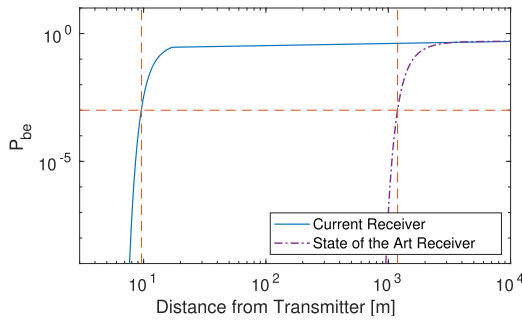
FIGURE 23. Projected BER performance over distance based on experimentally determined E_b/N_0 in two cases: i) using the current *B*-field sensor, and ii) using the much larger AWESOME *B*-field receiver. The horizontal line denotes $P_{be} = 10^{-3}$.

including the erroneous symbol, successful transmission of the message is completed.

D. BIT ERROR RATE (BER) ANALYSIS OF THE PROTOTYPE

Using the data collected in the previous section with the receiver placed 4.67 m away from the prototype transmitter, E_b/N_0 for the channel is measured to be 13.67 dB, which corresponds to a negligible BER of $P_{be} = 2.5 \times 10^{-22}$. In practice, a single symbol error was observed out of 416 symbols in the received message, which is promising but insufficient for estimating BER.

As magnetic field strength drops off as $B_{dip} \propto 1/r^3$ and $E_b = (A_s^2 \, T_s)/\log_2(M)$ in a non-conductive medium, the bit energy $E_b \propto 1/r^6$. This relationship is used to predict BER performance versus distance within such media by using the prototype mechanical transmitter. The field strength observed over distance in air (see Fig. 13) is consistent with simulations for a magnetic dipole. The expected BER performance of the prototype is extrapolated using this trend.

We define the theoretical maximum transmit distance as the distance where P_{be} reaches a value of 10^{-3}. This is generally considered to be a reasonable upper limit for message transmission without additional error correction. For the present receiver, this occurs at a distance of 9.6 m, as shown in Fig. 23. However, significantly longer-range communications are possible with a more sensitive *B*-field sensor. For example, let us consider the state-of-the-art ELF sensor used in the well-known AWESOME instrument [17]. This device uses a much larger detector (area = 1.69 m^2), resulting in a low input-referred noise of $\sim$40 fT/Hz$^{1/2}$ at 100 Hz. In this case, the expected useful range of the transmitter increases to 1.19 km, as shown in Fig. 23.

E. ENERGY CONSUMPTION WITH CP-FSK AND CF-FSK

The energy consumption of CP-FSK and CF-FSK transmission was compared using the prototype transmitter. Three runs of 100 randomly generated symbols were transmitted with a bit period of 0.5 seconds and $M = 15$ symbols using both schemes. Each transmission was performed twice. Results are tabulated in Table 1. No significant difference

TABLE 1. Comparison of energy consumption for 100-symbol transmit sequences using FSK, CP-FSK, and CF-FSK modulation schemes.

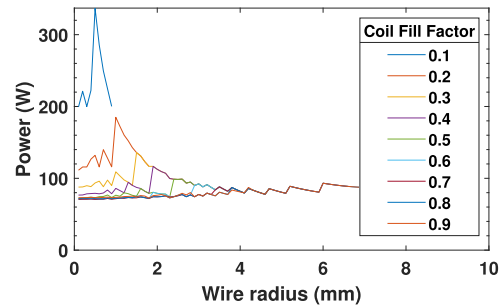| Data Set	Energy Consumption (Joules)		
	FSK	CP-FSK	CF-FSK
1	1223	1171	1192
	1190	1191	1181
2	1183	1274	1265
	1177	1271	1264
3	1176	1132	1130
	1182	1130	1127

FIGURE 24. Simulated power consumption (at 100 Hz) of an inductive coil with the same outer dimensions and magnetic moment as the mechanical ELF transmitter. Plots are shown for various values of fill factor ρ, where $1 - \rho$ is the ratio of inner to outer diameter for the coil.

between the schemes is observed in this data. This is because the non-optimized mechanical design of our prototype results in the load torque being much larger than the modulation torque (i.e., ensures that $\tau_L \gg \tau_{mod}$).

From the data in Table 1, average power consumption of the prototype mechanical transmitter is 11.0 W during operation. We compare this with the power required to generate an equivalent dipole field (with identical $1/r^3$ drop-off versus distance) using an electrical coil with the same dimensions as the prototype transmitter. In Fig. 24, we simulate the power required to generate an equivalent field with an electrical coil of varied fill factor. For fill factors of 0.4-0.9, the power required is about 75 W, or 6-7$\times$ the power used by the proposed prototype. These estimates are to be taken as lower bounds. The comparison does not account for the efficiency of the driver in each case, current crowding (proximity effect) or the thickness of the insulation in an electrical coil, or torque between elements in a distributed array of permanent dipoles.

F. EFFECTS OF NON-RANDOM DATA

Transmission of data by FSK modulation is affected by limited channel bandwidth. For example, in our case frequency deviations must remain smaller than $\pm$20 Hz to avoid 120 Hz interference. As a result, it is not possible to transmit long sequences of multiple bits with the same sign, as may occur in non-random data. To illustrate the problem, consider the case of the $M = 4$ level CP-FSK waveform used to transmit data with the prototype transmitter. The signal corresponding
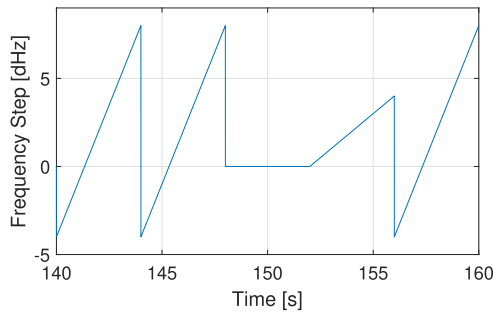
FIGURE 25. Sequence of 5 non-random CP-FSK bits showing required frequency discontinuities for data transmission.
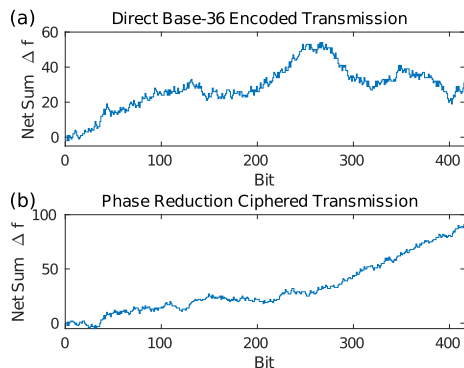

FIGURE 26. Comparison of accumulated frequency shift for non-random data: (a) original data, and (b) with a phase reduction cipher.

to five transmitted bits from the encoded excerpt of Shakespeare's Hamlet are shown in Fig. 25. The first bit is a $+3$, which may only be transmitted as a transition from the lowest FSK level to the highest level. At the highest level, a smooth transition could be used to transmit 0, -1, -2, or -3, but the next bit in the sequence is also $+3$. Therefore a discontinuity is required to limit transmit bandwidth, as shown. This behavior is compared to the ideal nature of the transition between bits 3 and 4 in the sample, which is a smooth transition. The transition from bit 3 to bit 4 would have lower τ_{mod} than the transition from bit 1 to 2.

Data transmission would be most power efficient if there were no frequency discontinuities such as those shown in Fig. 25. This is only feasible for random data. Non-random data will frequently require transmission of multiple repeated positive or negative values which results in discontinuities shown in the figure. This problem is visualized by plotting the accumulated frequency shift Δf across the number of transmitted bits in a sample 208-byte sequence of the previously described experiment. Fig. 26(a) shows that the accumulated frequency shift can reach relatively large values. One proposed fix was to employ a substitution cipher before data encoding from base-36, assigning the most commonly used characters to average zero or low shift bytes. For example, assigning the most common letters in the English language, namely 'e', 't', and 'a', to transmit bytes $(0,0)$, $(+1,-1)$, and $(-1,+1)$ respectively. The result of applying this cipher is shown in Fig. 26(b). Control and special character bits

in the original encoding scheme were assigned to values beginning with $+3$, and were not changed by the cipher. As a result, the control bits cause a net positive accumulation of frequency shift over time which is not removed by the phase reduction cipher. The cipher is seen to be effective at removing some of the non-random shift caused by characters A-Z.

VI. SAMPLE DATA ENCODING

Here is presented the same message transmitted in the long-duration message transmission experiments, followed by the steps applied to produce the transmission signal $m(t)$. The transmitted message is the following 233 characters with no new-line encoding.

```
WHAT A PIECE OF WORK IS MAN!
HOW NOBLE IN REASON,
HOW INFINITE IN FACULTY.
IN FORM AND MOVING,
HOW EXPRESS AND ADMIRABLE.
IN ACTION, HOW LIKE AN ANGEL.
IN APPREHENSION, HOW LIKE A GOD.
THE BEAUTY OF THE WORLD,
THE PARAGON OF ANIMALS.
```

The Burrows-Wheeler transform is applied to the data. The first step of this transform is to add beginning and end of sequence markers, shown here as '/' and 'ŕespectively. This increases the length of the output by two for a total of 235 characters to be transmitted.

```
/.ETNDESMNFNEWNNA,,,,!..E.
EWKWWSDWNYEEAN.,FFENGNNNDS
ELYD  R F RM M     PEHE OA
EAANNLOAKKHTLCHHLRBIRGHR O
OO N NN AWTTTE       PLLN
VFSTM NRIIERBB  AURI D
IAIIIOIAOOOAAIIAAI ENG   G
SIIWWFMHHHHH  APXIA PPOOOS
ILNAEAI   CULCAOOOOOO\  ETT
```

Compression is applied using run length encoding. To visualize the effect, the run-counter character is written explicitly as (xN) where N is the number of times the previous character is repeated in the uncompressed sequence. Each counter is expressed as a single special character in the implemented reduced character set. The result is a sequence of 208 characters.

```
/.ETNDESMNFNEWN(x2)A,(x4)!.(x2)
E.EWKW(x2)SDWNYE(x2)AN.,F(x2)EN
GN(x3)DSELYD(x2)R F RM M(x5)PEH
E OAEA(x2)N(x2)LOAK(x2)HTLCH(x2)
LRBIRGHR O(x3) N N(x2) AWT(x3)
E(x5)PL(x2)N(x6)VFSTM NRI(x2)ER
B(x2)(x2)AURI D IAI(x3)OIAO(x3)
A(x2)I(x2)A(x2)I ENG(x3)GSI(x2)
W(x2)FMH(x5)(x2)APXIA P(x2)O(x3)
SILNAEAI(x3)CULCAO(x6)\(x2)ET(x2)
```

Finally each character is encoded to two bit bytes using septenary bits. The resulting stream is 208 bytes transmitted as 416 bits.

```
1606224535212244343523352252356114
3663460661220622523252614421523554
2261143506362361223524356221442233
5421606143602360433460346064412225
2260401422146135613340143261254533
2025613343153043242543604062603560
3561601452456222606441336135606551
2344453460354330612243156160611450
4330602160301430624030144062146130
6114613060223524606224443061526123
3425646061144153301460416140624430
3335142214306062205033201440652660
61224561
```

Using $T_s = 4$ s, this sequence takes 1664 seconds or 27 m 44 s. Implementing 8Y0 (8 data bits, one parity bit, zero stop bits) would increase the size of transmissions by a factor of $\frac{9}{8}$, here resulting in 468 bits instead of 416 for a 12.5% increase in transmission time, up to 1872 s (31 m 12 s).

VII. CONCLUSION

We have described the design of miniaturized power-efficient ELF transmitters based on the mechanical rotation of permanently-polarized dipoles. The latter can use permanent magnets (ferromagnets, suitable for ELF) or electrets (ferroelectrics, suitable for VLF) [2]. The moment of inertia of the rotating dipoles must be minimized to reduce peak electrical power and increase the data rate. The use of a distributed array of $N > 1$ sub-elements minimizes overall inertia, while long and thin cylinders are optimal geometries for minimizing the inertia of each sub-element. However, such elongated shapes are difficult to manufacture in practice. The high-speed rotation of the magnetized cylinders is also accompanied by formidable mechanical design challenges (balancing, dynamic stability, etc.), which will be addressed in future work.

An ELF transmitter constructed using a mechanically-rotating magnetic dipole was evaluated to demonstrate its use for non-line-of-sight wireless communications in conductive media. Data was successfully transmitted through walls and floors, in particular from inside a laboratory to a hallway on a different floor of the building. Design challenges were considered for the receiver, including the impact of power line interference on the effectiveness of long-range data transmission. Future work will focus on improved receiver designs to maximize the useful transmission range.

APPENDIX
SAMPLE DATA ENCODING

Here is presented the same message transmitted in the long-duration message transmission experiments, followed by the steps applied to produce the transmission signal $m(t)$.

The transmitted message is the following 233 characters with no new-line encoding.

```
WHAT A PIECE OF WORK IS MAN!
HOW NOBLE IN REASON,
HOW INFINITE IN FACULTY.
IN FORM AND MOVING,
HOW EXPRESS AND ADMIRABLE.
IN ACTION, HOW LIKE AN ANGEL.
IN APPREHENSION, HOW LIKE A GOD.
THE BEAUTY OF THE WORLD,
THE PARAGON OF ANIMALS.
```

The Burrows-Wheeler transform is applied to the data. The first step of this transform is to add beginning and end of sequence markers, shown here as '/' and 'respectively. This increases the length of the output by two for a total of 235 characters to be transmitted.

```
/.ETNDESMNFNEWNNA,,,,!..E.
EWKWWSDWNYEEAN.,FFENGNNNDS
ELYD  R F RM M     PEHE OA
EAANNLOAKKHTLCHHLRBIRGHR O
OO N NN AWTTTE      PLLN
VFSTM NRIIERBB  AURI D
IAIIIOIAOOOAAIIAAI ENG   G
SIIWWFMHHHHH  APXIA PPOOOS
ILNAEAI   CULCAOOOOOO\  ETT
```

Compression is applied using run length encoding. To visualize the effect, the run-counter character is written explicitly as (xN) where N is the number of times the previous character is repeated in the uncompressed sequence. Each counter is expressed as a single special character in the implemented reduced character set. The result is a sequence of 208 characters.

```
/.ETNDESMNFNEWN(x2)A,(x4)!.(x2)
E.EWKW(x2)SDWNYE(x2)AN.,F(x2)EN
GN(x3)DSELYD(x2)R F RM M(x5)PEH
E OAEA(x2)N(x2)LOAK(x2)HTLCH(x2)
LRBIRGHR O(x3) N N(x2) AWT(x3)
E(x5)PL(x2)N(x6)VFSTM NRI(x2)ER
B(x2)(x2)AURI D IAI(x3)OIAO(x3)
A(x2)I(x2)A(x2)I ENG(x3)GSI(x2)
W(x2)FMH(x5)(x2)APXIA P(x2)O(x3)
SILNAEAI(x3)CULCAO(x6)\(x2)ET(x2)
```

Finally each character is encoded to two bit bytes using septenary bits. The resulting stream is 208 bytes transmitted as 416 bits.

```
1606224535212244343523352252356114
3663460661220622523252614421523554
2261143506362361223524356221442233
5421606143602360433460346064412225
2260401422146135613340143261254533
2025613343153043242543604062603560
3561601452456222606441336135606551
```

```
2344453460354330612243156160611450
4330602160301430624030144062146130
6114613060223524606224443061526123
3425646061144153301460416140624430
3335142214306062205033201440652660
61224561
```

Using $T_s = 4$ s, this sequence takes 1664 seconds or 27 m 44 s. Implementing 8Y0 (8 data bits, one parity bit, zero stop bits) would increase the size of transmissions by a factor of $\frac{9}{8}$, here resulting in 468 bits instead of 416 for a 12.5% increase in transmission time, up to 1872 s (31 m 12 s).

REFERENCES

[1] M. T. B. Tarek, S. Dharmasena, A. Madanayake, S. Choi, J. Glickstein, J. Liang, and S. Mandal, "Power-efficient data modulation for all-mechanical ULF/VLF transmitters," in *Proc. IEEE 61st Int. Midwest Symp. Circuits Syst. (MWSCAS)*, Aug. 2018, pp. 759–762.

[2] A. Madanayake, S. Choi, M. Tarek, S. Dharmasena, S. Mandal, J. Glickstein, and A. Sehirlioglu, "Energy-efficient ULF/VLF transmitters based on mechanically-rotating dipoles," in *Proc. Moratuwa Eng. Res. Conf. (MERCon)*, May 2017, pp. 230–235.

[3] A. Singh and S. Sharma, "Interpretation of very low frequency electromagnetic measurements in terms of normalized current density over variable topography," *J. Appl. Geophys.*, vol. 133, pp. 82–91, Oct. 2016.

[4] U. S. Inan, "VLF heating of the lower ionosphere," *Geophys. Res. Lett.*, vol. 17, no. 6, pp. 729–732, 1990.

[5] M. Hayakawa, "VLF/LF radio sounding of ionospheric perturbations associated with earthquakes," *Sensors*, vol. 7, no. 7, pp. 1141–1158, 2007.

[6] M. C. Domingo, "Magnetic induction for underwater wireless communication networks," *IEEE Trans. Antennas Propag.*, vol. 60, no. 6, pp. 2929–2939, Jun. 2012.

[7] K. Hansson and B. Greenebaum, "Environmental and occupationally encountered electromagnetic fields," in *Bioengineering and Biophysical Aspects of Electromagnetic Fields*. Oct. 2018, ch. 1–34.

[8] L. J. Chu, "Physical limitations of omni-directional antennas," *J. Appl. Phys.*, vol. 19, no. 12, pp. 1163–1175, 1948.

[9] R. F. Harrington, "Effect of antenna size on gain, bandwidth, and efficiency," *J. Res. Nat. Bur. Standards*, vol. 64D, no. 1, pp. 1–12, Jan./Feb. 1960.

[10] H. Wheeler, "Small antennas," *IEEE Trans. Antennas Propag.*, vol. AP-23, no. 4, pp. 462–469, Jul. 1975.

[11] H. Rowe, "Extremely low frequency (ELF) communication to submarines," *IEEE Trans. Commun.*, vol. 22, no. 4, pp. 371–385, Apr. 1974.

[12] E. Field, L. Kies, P. Bannister, R. Ingram, W. Hopkins, and M. Roberts, "An aerostat-supported ELF/VLF transmitter," *Radio Sci.*, vol. 24, no. 2, pp. 235–246, 1989.

[13] R. Barr, W. Ireland, and M. J. Smith, "ELF, VLF and LF radiation from a very large loop antenna with a mountain core," *IEE Proc. H Microw., Antennas Propag.*, vol. 140, no. 2, pp. 129–134, Apr. 1993.

[14] S. Mandal, S. Utsuzawa, D. Cory, M. Hürlimann, M. Poitzsch, and Y.-Q. Song, "An ultra-broadband low-frequency magnetic resonance system," *J. Magn. Reson.*, vol. 242, pp. 113–125, May 2014.

[15] A. J. Smith, "VELOX: A new VLF/ELF receiver in Antarctica for the global geospace science mission," *J. Atmos. Terr. Phys.*, vol. 57, no. 5, pp. 507–524, 1995.

[16] S. K. Harriman, E. W. Paschal, and U. S. Inan, "Magnetic sensor design for femtotesla low-frequency signals," *IEEE Trans. Geosci. Remote Sens.*, vol. 48, no. 1, pp. 396–402, Jan. 2010.

[17] M. B. Cohen, U. S. Inan, and E. W. Paschal, "Sensitive broadband ELF/VLF radio reception with the AWESOME instrument," *IEEE Trans. Geosci. Remote Sens.*, vol. 48, no. 1, pp. 3–17, Jan. 2010.

[18] X. Xu and Y. E. Wang, "Beyond the efficiency bandwidth limit with switched electrically small antennas," in *Proc. IEEE Antennas Propag. Soc. Int. Symp.*, Jun. 2007, pp. 2261–2264.

[19] U. Azad and Y. E. Wang, "Direct antenna modulation (DAM) for enhanced capacity performance of near-field communication (NFC) link," *IEEE Trans. Circuits Syst. I, Reg. Papers*, vol. 61, no. 3, pp. 902–910, Mar. 2014.

[20] V. J. Phillips, "The Alexanderson alternator," *Eng. Sci. Educ. J.*, vol. 6, no. 1, pp. 37–42, Feb. 1997.

[21] DARPA. *A Mechanical Based Antenna (AMEBA)*. Accessed: Dec. 19, 2016. [Online]. Available: https://govtribe.com/opportunity/federal-contract-opportunity/a-mechanical-based-antenna-ameba-hr001117s0007

[22] S. Gong, Y. Liu, and Y. Liu, "A rotating-magnet based mechanical antenna (RMBMA) for ELF-ULF wireless communication," *Prog. Electromagn. Res. M*, vol. 72, pp. 125–133, Aug. 2018.

[23] H. C. Burch, A. Garraud, M. F. Mitchell, R. C. Moore, and D. P. Arnold, "Experimental generation of ELF radio signals using a rotating magnet," *IEEE Trans. Antennas Propag.*, vol. 66, no. 11, pp. 6265–6272, Nov. 2018.

[24] M. A. Kemp, M. Franzi, A. Haase, E. Jongewaard, M. T. Whittaker, M. Kirkpatrick, and R. Sparr, "A high Q piezoelectric resonator as a portable VLF transmitter," *Nature Commun.*, vol. 10, Apr. 2019, Art. no. 1715.

[25] J. Xu, C. M. Leung, X. Zhuang, J. Li, S. Bhardwaj, J. Volakis, and D. Viehland, "A low frequency mechanical transmitter based on magnetoelectric heterostructures operated at their resonance frequency," *MDPI Sensors*, vol. 19, no. 4, p. 853, Feb. 2019.

[26] C. Zwyssig, S. D. Round, and J. W. Kolar, "Analytical and experimental investigation of a low torque, ultra-high speed drive system," in *Proc. IEEE Ind. Appl. Conf.*, vol. 3, Oct. 2006, pp. 1507–1513.

[27] H. H. Jeffcott, "XXVII. The lateral vibration of loaded shafts in the neighbourhood of a whirling speed—The effect of want of balance," *London, Edinburgh, Dublin Philos. Mag. J. Sci.*, vol. 37, no. 219, pp. 304–314, 1919.

[28] E. Swanson, C. D. Powell, and S. Weissman, "A practical review of rotating machinery critical speeds and modes," *Sound Vib.*, vol. 39, no. 5, pp. 16–17, May 2005.

[29] J. W. Dixon and M. E. Ortuzar, "Ultracapacitors + DC–DC converters in regenerative braking system," *IEEE Aerosp. Electron. Syst. Mag.*, vol. 17, no. 8, pp. 16–21, Aug. 2002.

[30] J. B. Anderson, T. Aulin, and C.-E. Sundberg, *Digital Phase Modulation* (Applications of Communications Theory). New York, NY, USA: Plenum Press, 1986.

[31] L. W. Couch, II, *Digital and Analog Communication Systems*, 4th ed. New York, NY, USA: Macmillan Publishers, 1993.

[32] D. Salomon, *Data Compression: The Complete Reference*. New York, NY, USA: Springer, 2004.

[33] J. Ziv and A. Lempel, "A universal algorithm for sequential data compression," *IEEE Trans. Inf. Theory*, vol. 23, no. 3, pp. 337–343, May 1977.

[34] A. Goldsmith, *Wireless Communications*. Cambridge, U.K.: Cambridge Univ. Press, 2005.

[35] P. D. Welch, "The use of fast Fourier transform for the estimation of power spectra: A method based on time averaging over short, modified periodograms," *IEEE Trans. Audio Electroacoust.*, vol. 15, no. 2, pp. 70–73, Jun. 1967.

[36] J. R. Carson, "Notes on the theory of modulation," *Proc. Inst. Radio Eng.*, vol. 10, no. 1, pp. 57–64, Feb. 1922.

[37] S. L. Bernstein, M. L. Burrows, J. E. Evans, A. S. Griffiths, D. A. McNeill, C. W. Niessen, I. Richer, D. P. White, and D. K. Willim, "Long-range communications at extremely low frequencies," *Proc. IEEE*, vol. 62, no. 3, pp. 292–312, Mar. 1974.

JARRED S. GLICKSTEIN (S'16) received the B.S. and M.S. degrees in electrical engineering from Case Western Reserve University, Cleveland, OH, USA, in 2016 and 2018, respectively, where he is currently pursuing the Ph.D. degree in electrical engineering.

He was a Research Assistant with the Center for Global Health and Diseases, Case Western Reserve University, in 2015, where he has been a Research Assistant with the Integrated Circuits and Sensor Physics Lab, since 2015. His research interests include analog sensors and instrumentation design, electromechanical devices, experiment automation, and novel applications in magnetic materials.
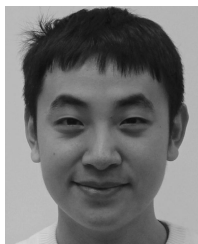
JIFU LIANG (M'16) received the B.E. degree in optoelectronic information engineering from the Huazhong University of Science and Technology, Wuhan, China, in 2014, and the M.S. degree in electrical engineering from Case Western Reserve University, Cleveland, OH, USA, in 2016, where he is currently pursuing the Ph.D. degree in electrical engineering.

He is currently a Research Assistant with the Integrated Circuits and Sensor Physics Lab, Case Western Reserve University. His research interests include integrated circuits for biomedical and array processing applications.

ARJUNA MADANAYAKE (SM'08) received the B.Sc. degree (Hons.) in electronic and telecommunication engineering from the University of Moratuwa, Moratuwa, Sri Lanka, in 2002, and the M.Sc. and Ph.D. degrees in electrical engineering from the University of Calgary, Calgary, AB, Canada, in 2004 and 2008, respectively.

He is currently an Associate Professor with the Department of Electrical and Computer Engineering, Florida International University, Miami, FL, USA. His research interests include multidimensional signal processing, analog/digital and mixed-signal electronics, and VLSI for fast algorithms.
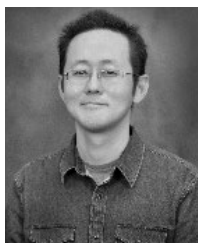
SEUNGDEOG CHOI (S'07–M'12–SM'16) received the B.S. degree in electrical and computer engineering from Chung-Ang University, in 2004, the M.S. degree from Seoul National University, South Korea, in 2006, and the Ph.D. degree in electric power and power electronics from Texas A&M University, College Station, in 2010.

He was with LG Electronics, Seoul, South Korea, from 2006 to 2007, and a Research Engineer with Toshiba International Corp., Houston, TX, USA, from 2009 to 2012. He was an Assistant Professor with The University of Akron, from 2012 to 2018. He has been an Associate Professor with Mississippi State University, Starkville, since 2018. He has coauthored a book. He has published more than 100 articles including journal articles (published/under review). He has published more than 100 articles in around 90 peer-reviewed IEEE conferences. He holds around 20 patents (registered/pending). His research interests include degradation modeling, fault tolerant control, and the fault tolerant design of electric machines, power electronics, battery, solar panel, and wider vehicular/aircraft microgrid systems.

SOUMYAJIT MANDAL (S'01–M'09–SM'14) received the B.Tech. degree in electronics and electrical communications engineering from IIT Kharagpur, India, in 2002, and the M.S. and Ph.D. degrees in electrical engineering from the Massachusetts Institute of Technology (MIT), Cambridge, MA, USA, in 2004 and 2009, respectively.

He was a Research Scientist with Schlumberger-Doll Research, Cambridge, MA, USA, from 2010 to 2014. He is currently an Assistant Professor with the Department of Electrical Engineering and Computer Science, Case Western Reserve University, Cleveland, OH, USA. He has over 60 publications in peer-reviewed journals and premier conferences. His research interests include analog and biological computation, magnetic resonance sensors, low-power analog and RF circuits, and precision instrumentation for various biomedical and sensor interface applications. He was a recipient of the President of India Gold Medal, in 2002, delivered the Annual MIT Microsystems Technology Laboratories Doctoral Dissertation Seminar in recognition of outstanding research of interest to a broad audience, in 2009, and the T. Keith Glennan Fellowship, in 2016.

• • •